Journal of Solid State Chemistry 276 (2019) 181–189

Contents lists available at ScienceDirect

Journal of Solid State Chemistry

journal homepage: www.elsevier.com/locate/jssc

Phase stability and thermoelectric properties of TiCoSb-TiM_2Sn (M = Ni, Fe) Heusler composites

M. Asaad [a], J. Buckman [b], R.I. Smith [c], J.-W.G. Bos [a,*]

[a] Institute of Chemical Sciences and Centre for Advanced Energy Storage and Recovery, School of Engineering and Physical Sciences, Heriot-Watt University, Edinburgh, EH14 4AS, UK
[b] Institute of Petroleum Engineering, Heriot-Watt University, Edinburgh, EH14 4AS, UK
[c] ISIS Facility, STFC Rutherford Appleton Laboratory, Harwell Campus, Didcot, OX11 0QX, UK

ARTICLE INFO

Keywords:
Half-Heusler alloys
Thermoelectric
TiCoSb

ABSTRACT

Heusler composites have attracted significant attention as a new route towards improving the thermoelectric figure of merit (ZT) through reduction of the lattice thermal conductivity and carrier filtering effects. This work extends this field by investigating TiCoSb-TiM_2Sn (M = Ni, Fe) composites. All end-members are stable phases but no clean segregation into half- and full-Heusler phases was observed. Instead, for M = Ni, partial substitution on the Co sublattice and n-type doping occurs, combined with the formation of Ni_3Sn_2 and full-Heusler phases. For M = Fe, substitution on the Co site occurs, leading to p-type conduction. Rietveld analysis of neutron powder diffraction data reveals no evidence for the presence of metals on the vacant tetrahedral site, signalling the absence of embedded Heusler inclusions. The thermoelectric properties of both series vary systematically with composition. For both n-type (M = Ni) and p-type (M = Fe) series, the highest measured power factors $S^2/\rho \sim 0.8\ mW\ m^{-1}\ K^{-2}$ leading to ZT ~ 0.12 at 713 K. This work extends knowledge regarding the phase stability and thermoelectric properties of TiCoSb-based Heusler composites.

1. Introduction

Electricity generation using thermoelectric technology is an attractive route to increase the efficiency of heat generating processes [1,2]. Application has so far been limited due to the difficulties in finding materials with a good trade-off between performance, stability and cost. Half-Heusler (HH) alloys work well at mid-range temperatures ($T \leq 300$–$800\ ^\circ C$), contain relatively abundant elements and have good mechanical and temperature stability [3–5]. They are characterised by large power factors S^2/ρ but are limited by relatively large thermal conductivities $\kappa = 3$–$4\ W\ m^{-1}\ K^{-1}$, leading to figures of merit, $ZT = (S^2/\rho\kappa)T = 1$–$1.5$ for the best compositions [5]. Here, S is the Seebeck coefficient, ρ is the electrical resistivity and κ is the sum of the lattice (κ_{lat}) and electronic (κ_{el}) thermal conductivities. Historically, n-type XNiSn and p-type XCoSb-based compositions (X = Ti, Zr and Hf) have attracted most attention with ZT = 1–1.5 in optimised samples [6–9]. Recently, a range of other compositions including NbFeSb (p-type) [10,11] $Nb_{0.8}CoSb$ (n-type) [12,13] and ZrCoBi (p-type) [14] have been shown to have $ZT \geq 1$ values. This has significantly expanded the range of HHs currently under investigation.

This manuscript is focused on TiCoSb, which is of interest because it is based on abundant elements and does not use Zr or Hf [15,16]. However, exploitation of p-type TiCoSb is challenging as it has smaller power factors, $S^2/\rho \sim 1.5\ mW\ m^{-1}\ K^{-2}$ [17–22], compared to the best p-type (Zr,Hf)CoSb HHs ($S^2/\rho \sim 3\ mW\ m^{-1}\ K^{-2}$) [4,8,9,23,24]. In addition, due to the lower mass and larger velocity of sound, $\kappa_{300K} \sim 18\ W\ m^{-1}\ K^{-1}$ for TiCoSb [25], whereas it is $\sim 4\ W\ m^{-1}\ K^{-1}$ for optimised (Zr,Hf)CoSb HHs with heavier atoms and significant mass disorder phonon scattering [8].

One possible route to improve the thermoelectric performance of TiCoSb is through formation of composites with full-Heusler (FH) phases [3]. HH-FH composites based on XNiSn-XNi_2Sn and XCoSb-XCo_2Sb have been reported to have improved S^2/ρ due to carrier filtering, as well as reductions in κ_{lat} originating from phonon scattering from embedded inclusions [26,27]. In most instances, there is little solubility of excess metals in the HH structure (e.g. Ni in ZrNiSn), and segregation into HH and FH phases is favoured [28]. The exact nature of the microstructure is dependent on the synthesis protocol and the observation of FH inclusions is not consistent across all reports [29–33]. Our work on $TiNiM_ySn$ HHs (M = Co, Ni and Cu), prepared using direct reactions between elemental powders at 900 °C, revealed a small solubility of excess metals (≤12%)

* Corresponding author.
E-mail address: j.w.g.bos@hw.ac.uk (J.-W.G. Bos).

https://doi.org/10.1016/j.jssc.2019.04.041
Received 22 February 2019; Received in revised form 26 April 2019; Accepted 28 April 2019
Available online 4 May 2019

on the vacant tetrahedral site of the TiNiSn structure [34,35]. These are present as randomly distributed interstitials and are effective at reducing κ_{lat}, leading to improvements in ZT [36–38]. In addition to the HH phases with interstitials, these samples contain larger sized FH domains with distinct peaks in diffraction patterns.

This manuscript is focused on the TiCoSb-TiM_2Sn (M = Fe, Ni) Heusler composites. The M = Fe and Ni FH end-members are stable and were chosen to create p- and n-type materials [39,40]. This was based on our work on the $TiNiM_ySn$ [TiNiSn-Ti$(Ni_{0.5}M_{0.5})_2$Sn] HH-FH composites, where M = Co with one less valence electron than Ni yielded p-type behaviour and M = Cu with an additional valence electron was found to be an efficient n-type dopant [34,37]. The current series can also be expressed as $TiCo_{1-x}M_{2x}Sb_{1-x/2}Sn_{x/2}$ to reflect its composition but we will use the $(TiCoSb)_{1-x}(TiM_2Sn)_x$ (M = Fe, Ni and $x \leq 0.2$) notation throughout this manuscript.

2. Experimental

Polycrystalline $(TiCoSb)_{1-x}(TiM_2Sn)_x$ (M = Fe or Ni; $x \leq 0.2$) samples were prepared on a 3-gram scale by reaction of elemental precursors. Metal powders of Ti (−325 mesh, Alfa Aesar, 99.99%), Co (1.6 μm, Alfa Aesar, 99.8%), Sb (powdered shots, Alfa Aesar, 99.99%), Sn (−100 mesh, Alfa Aesar, 99.85%), Fe (<10 μm, Alfa Aesar, 99.5%) and Ni (−120 mesh Alfa Aesar, 99.99%) were used as starting materials. Stoichiometric amounts of the constituent elements were mixed using an agate mortar and pestle, cold pressed into pellets and wrapped in Ta foil (0.025 mm thickness, Sigma Aldrich). Samples were initially annealed under vacuum in quartz tubes at 850 °C for 24 h, then reground, cold pressed, wrapped in Ta foil, and annealed for a further 12 days at 850 °C. The resulting products were then subjected to a densification step using hot pressing at temperatures (850 °C ≤ T ≤ 885 °C) for 20 min under 80 MPa. The densities (d) of the hot-pressed samples were calculated from their weight and dimensions. Laboratory X-ray powder diffraction (XRPD) patterns were obtained for all samples on a Bruker D8 advance diffractometer using Cu $K_{\alpha 1}$ radiation over the range $10^\circ \leq 2\theta \leq 120^\circ$ for a period of 8 h. No significant changes were observed before and after hot pressing. Time-of-flight neutron powder diffraction (NPD) data were collected at room temperature from ~1.5 g of finely ground samples using the upgraded Polaris diffractometer at the ISIS Neutron and Muon Source, Rutherford Appleton Laboratory, UK. Powdered samples were loaded into cylindrical vanadium sample cans and diffraction patterns accumulated for ~250 μAh proton beam current to the ISIS target, corresponding to ~1½ hours for each sample. Rietveld analysis of diffraction data was carried out using the GSAS and EXPGUI programmes [41,42]. Rectangular bars were cut from the hot-pressed disks, and electrical resistivity and Seebeck coefficient measurements were made using a Linseis LSR-3 instrument under a He atmosphere. Thermal diffusivity measurements (α) were carried out using a Linseis LFA 1000 laser flash instrument. The thermal conductivity $\kappa = \alpha C_p d$ was calculated using the experimental α and d values and heat capacity data (C_p) for TiCoSb [43]. A porosity correction; $\kappa/\kappa_{dense} = 1\text{-}(4/3)\phi$, where ϕ is the porosity obtained from the sample density, was applied. The lattice thermal conductivity was calculated using $\kappa_{lat} = \kappa - LT/\rho$; where the Lorenz number, L was estimated using the procedure outlined in Ref. [44]. The homogeneity and chemical composition of two compositions; M = Ni, x = 0.1 and M = Fe, x = 0.2 was checked after thermal diffusivity measurements using a Quanta 650 FEG scanning electron microscope (SEM) operated at 20 kV in high vacuum mode and equipped with an Oxford Instruments X-max 150^N detector for Energy dispersive X-ray spectroscopy (EDX) mapping. Quantitative analysis of selected areas was performed using Aztec Large Area Maps software. The working distance, spot size and collecting time used were 10 mm, 4.5 and 75 + frames, respectively. Prior to SEM-EDX analysis, samples were polished to 0.5 μm roughness with Al_2O_3 sandpaper.

3. Results

Throughout the results sections, the n-type M = Ni series is discussed first, followed by the p-type M = Fe series.

3.1. X-ray powder diffraction

The XRPD patterns for the M = Ni samples (x = 0.05, 0.1, 0.15 and 0.2) are given in Fig. 1a. The main peaks are matched with those for a HH structure. Ni_3Sn_2 peaks are observed in the x = 0.1, 0.15 and 0.2 compositions, while an increasing amount of FH phase is evident in the patterns for x = 0.15 and 0.2. Rietveld analysis was used to obtain HH lattice parameters and revealed a similar a_{HH} ~5.888 Å for each composition (Table 1). The XRPD patterns for the M = Fe series (x = 0.05, 0.1, 0.15 and 0.2) are shown in Fig. 1b. In addition to the main HH reflections, only minor amounts of other phases are observed, including Sn, SbSn and Fe_2Sn. See Fig. 1b for full details. Surprisingly, no FH reflections were evident in any of the patterns. The HH lattice parameters were again found to be similar with a_{HH} ~5.886 Å (Table 1).

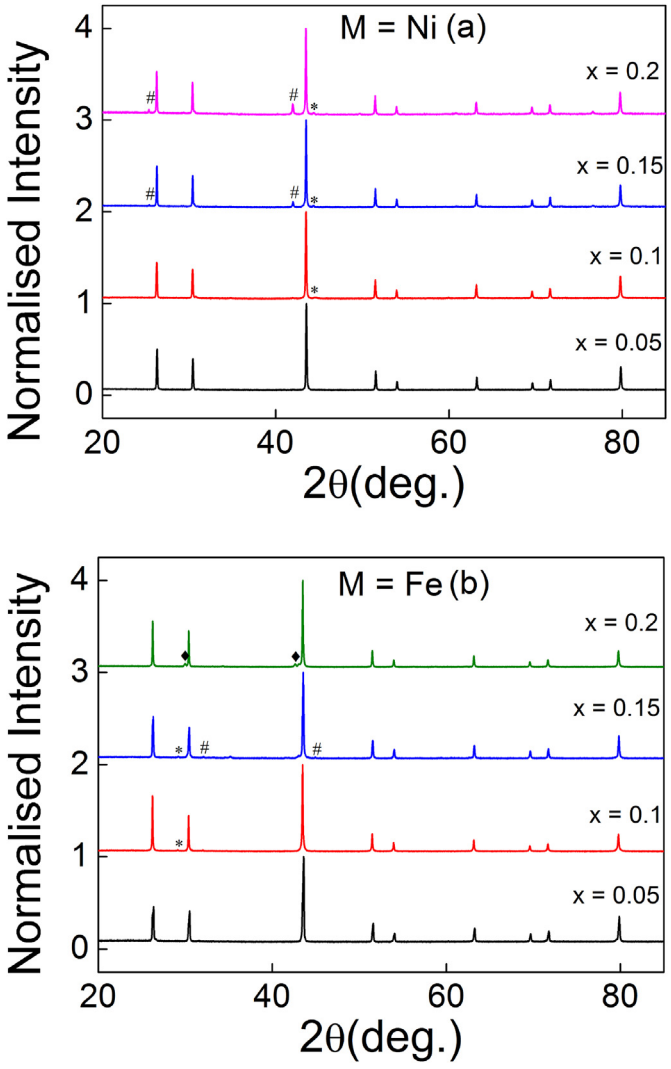

Fig. 1. Laboratory X-ray powder diffraction patterns for the M = Ni **(a)** and the M = Fe **(b)** $(TiCoSb)_{1-x}(TiM_2Sn)_x$ Heusler composites. Secondary phases for the M = Ni series are: Ni_3Sn_2 (*) and Full Heusler alloy (#). For the M = Fe series, small amounts of SbSn (*), Sn (#) and Fe_2Sn (◆) are observed.

Table 1
Half-Heusler phase lattice parameter (a) from X-ray powder diffraction, sample density, percentage density, 313 K electrical resistivity (ρ) and Seebeck coefficient (S) and maximum power factor (S^2/ρ) for the M = Ni and M = Fe $(TiCoSb)_{1-x}(TiMi_2Sn)_x$ Heusler composites.

x	a (Å)	Density ($g.cm^{-3}$)	% Density	ρ_{313k} (mΩ cm)	S_{313K} (μV K^{-1})	$(S^2/\rho)_{max}$ (mW m^{-1} K^{-2})
M = Ni						
0.05	5.8866(1)	6.2(1)	84(1)	11.6(6)	−184(9)	0.53(6)
0.10	5.8876(1)	6.8(1)	92(1)	6.0(3)	−142(7)	0.79(8)
0.15	5.8882(1)	6.9(1)	93(1)	4.0(2)	−113(6)	0.50(4)
0.20	5.8889(1)	7.0(1)	95(1)	1.80(9)	−67(3)	0.65(3)
M = Fe						
0.05	5.8849(1)	7.1(1)	96(1)	76(4)	−106(5)	0.05(1)
0.10	5.8849(1)	7.0(1)	95(1)	38(2)	176(9)	0.62(9)
0.15	5.8859(1)	7.2(1)	97(1)	4.2(2)	56(3)	0.43(3)
0.20	5.8870(1)	7.0(1)	95(1)	7.4(2)	112(6)	0.83(8)

3.2. Neutron powder diffraction

NPD data were collected from the M = Ni, x = 0.1, 0.15 and 0.2 samples. Rietveld analysis was used to obtain the experimental composition of the HH phases and gain further information on the secondary phases present. The obtained structural parameters are summarised in Table 2 and the quality of the fits is illustrated in Fig. 2. FH and Ni_3Sn_2 peaks are evident in the fits, which is consistent with the XRPD data discussed above. The TiCoSb HH structure has four interpenetrating face centred cubic lattices with Sb on 4a (0, 0, 0), Ti on 4b (½, ½, ½), Co on 4c (¼, ¼, ¼) and an empty 4d (¾, ¾, ¾) sublattice for stoichiometric TiCoSb. Partial occupancy of the 4d site is indicative of the presence of interstitial metals, while it could also signal embedded FH inclusions with the same lattice parameter as the matrix [32,34]. Transmission electron microscopy is needed to unambiguously distinguish these two scenarios [34]. Trial fits were attempted with Ni on the interstitial 4d and regular 4c (Co) sites. No evidence was found for any occupancy of the 4d-site, indicating the absence of interstitial metals or embedded inclusions. Note that the scattering contrast between Sb and Sn is small and does not allow for refinement of the Sb:Sn ratio on the 4a site. The final fits were performed

Table 2
Lattice parameters (a), weight percentages, thermal displacement parameters ($U_{iso}/Å^2$), fractional occupancies and fit statistics for the Rietveld fits to the Polaris neutron powder diffraction data from the M = Ni and M = Fe $(TiCoSb)_{1-x}(TiM_2Sn)_x$ Heusler composites.

M = Ni					M = Fe		
x		x = 0.1	x = 0.15	x = 0.2	x = 0.05	x = 0.10	x = 0.2
HH ($F\bar{4}3m$)					HH ($F\bar{4}3m$)		
a (Å)		5.8864(1)	5.8848(1)	5.8858(1)	5.8821(1)	5.8826(1)	5.8851(1)
wt (%)		94.9(1)	88.3(1)	85.0(1)	97.0(1)[a]	96.4(1)[b]	86.7(1)[c]
4b	U_{iso} ($Å^2$)	0.0041(1)	0.0041(1)	0.0043(1)	0.0040(1)	0.0039(1)	0.0043(1)
	Occ	Ti	Ti	Ti	Ti	Ti	Ti
4c	U_{iso} ($Å^2$)	0.0041(1)	0.0041(1)	0.0043(1)	0.0040(1)	0.0039(1)	0.0043(1)
	Occ	$Co_{0.87(1)}Ni_{0.13(1)}$	$Co_{0.87(1)}Ni_{0.13(1)}$	$Co_{0.84(1)}Ni_{0.16(1)}$	$Co_{0.91(1)}Fe_{0.09(1)}$	$Co_{0.97(1)}Fe_{0.03(1)}$	$Co_{0.91(1)}Fe_{0.09(1)}$
4a	U_{iso} ($Å^2$)	0.0041(1)	0.0041(1)	0.0043(1)	0.0040(1)	0.0039(1)	0.0043(1)
	Occ	$Sb_{0.9}Sn_{0.1}$	$Sb_{0.85}Sn_{0.15}$	$Sb_{0.8}Sn_{0.2}$	$Sb_{0.95}Sn_{0.05}$	$Sb_{0.9}Sn_{0.1}$	$Sb_{0.8}Sn_{0.2}$
4d	U_{iso} ($Å^2$)	–	–	–	–	–	–
	Occ	0	0	0	0	0	0
FH ($Fm\bar{3}m$)					FH ($Fm\bar{3}m$)		
a (Å)			6.0894(1)	6.0919(1)	–	–	–
wt (%)			5.7(1)	9.8(1)	–	–	–
4b	U_{iso} ($Å^2$)		0.0018(3)	0.0027(2)	–	–	–
	Occ		Ti	Ti	–	–	–
8c	U_{iso} ($Å^2$)		0.0140(3)	0.0148(1)	–	–	–
	Occ		$Ni_{1.93}$[d]	$Ni_{1.95}$[d]	–	–	–
4a	U_{iso} ($Å^2$)		0.0018(3)	0.0027(2)	–	–	–
	Occ		Sn	Sn	–	–	–
Ti_2O_3 ($R\bar{3}cH$)					Ti_2O_3 ($R\bar{3}cH$)		
a (Å)		5.150(1)	5.148(1)	5.135(1)	5.152(1)	5.147(1)	5.127(1)
c (Å)		13.598(2)	13.614(2)	13.690(2)	13.616(1)	13.635(2)	13.712(2)
wt (%)		1.0(1)	1.3(1)	1.1(1)	1.2(1)	1.0(1)	1.0(1)
	U_{iso} ($Å^2$)	0.008(1)	0.011(1)	0.006(1)	0.007(1)	0.007(1)	0.008(1)
Ni_3Sn_2 ($P6_3/mmc$)[e]					–		
a (Å)		4.0716(2)	4.0872(1)	4.0859(2)	–	–	–
c (Å)		5.1702(5)	5.1891(1)	5.1871(3)	–	–	–
wt (%)		4.1(1)	4.7(1)	4.1(1)	–	–	–
	U_{iso} ($Å^2$)	0.0102(4)	0.0115(4)	0.0098(3)	–	–	–
χ^2		2.08	1.28	3.10	1.03	1.45	4.73
wRp (%)	Bank 3	1.42	2.04	2.17	2.73	1.96	3.97
	Bank 4	1.63	2.19	2.60	2.50	2.31	3.64
	Bank 5	1.54	2.38	3.18	2.41	2.00	3.39
R_p (%)	Bank 3	2.13	3.14	2.81	4.30	2.45	5.99
	Bank 4	3.13	5.35	4.90	5.98	5.24	4.75
	Bank 5	4.51	7.55	4.94	8.63	5.33	5.48

[a] Sample contained 1.8(1)wt% of SbSn.
[b] Sample contained 1.8(1) wt % SbSn and 0.8(1) wt% FeCo.
[c] Sample contained 12.3(1) wt% Fe_2Sn phase (SG: $P6_3/mmc$; $a = 4.236$ Å, $c = 5.240$ Å; Fe1: (0, 0, 0), Fe/Ti2: (1/3, 2/3, 1/4), Sn: (1/3, 2/3, 3/4).
[d] Ni content estimated from the lattice parameter, using Ref. [34].
[e] Refinement of the Ni 2d-site occupancy suggests a composition of $Ni_{2.7}Sn_2$ for the x = 0.1 sample and Ni_3Sn_2 for the x = 0.15 and 0.2 samples.

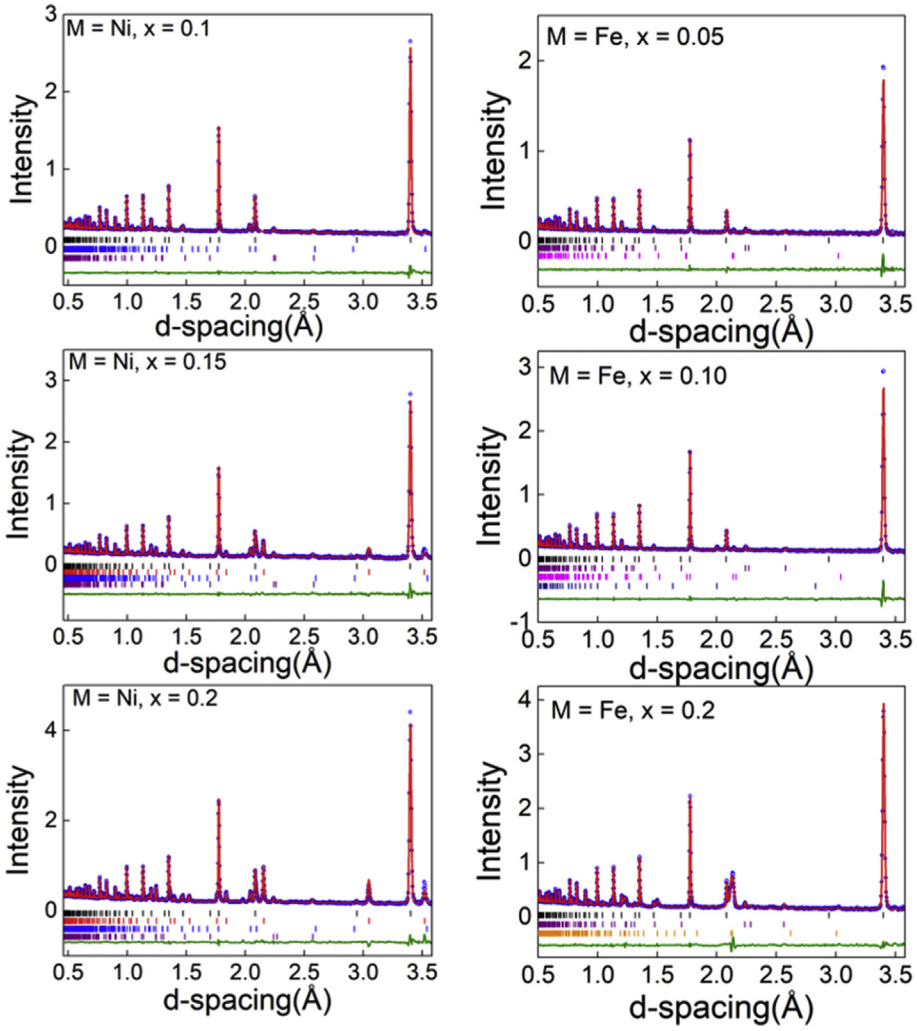

Fig. 2. Rietveld fitted powder neutron diffraction patterns for the M = Ni and M = Fe $(TiCoSb)_{1-x}(TiM_2Sn)_x$ Heusler composites. Blue circles are the observed data points, the red line is the calculated profile and the green line is the difference curve (obs-calc). Black vertical markers are for the HH phase, red markers are for the FH phase, blue markers are for Ni_3Sn_2, purple markers are for Ti_2O_3, magenta markers are for SbSn, navy markers are for FeCo and orange markers are for Fe_2Sn. Data shown are from the Polaris 90° detectors (bank 4) as this bank covers the full range of d-spacings observed from the phases present in the samples. (For interpretation of the references to colour in this figure legend, the reader is referred to the Web version of this article.)

with a model allowing the replacement of Co by Ni with the results summarised in Table 2. For x = 0.1 and 0.15, this leads to a refined Ni occupancy of 0.13(1), increasing to 0.16(1) for the x = 0.2 sample. These three samples have identical amounts of Ti_2O_3 (~1 wt%) and Ni_3Sn_2 (~4 wt%). There is no evidence for a FH phase for x = 0.1, while x = 0.15 and x = 0.2 have 5.7 wt% and 9.6 wt%, respectively. The observation of Ni_3Sn_2, rather than only FH phases, could be linked to the presence of Ti_2O_3, and reveals a deviation from the TiCoSb-$TiNi_2Sn$ tie-line in the phase diagram. We note that Ti_2O_3 and elemental Ti have a $\sqrt{3}$a x 3c relation between their unit cells [38].

For the M = Fe composites, NPD data were collected from the x = 0.05, 0.1 and 0.2 samples. The Rietveld fits are illustrated in Fig. 2 and the fitted structural and goodness of fit parameters are summarised in Table 2. NPD confirms the absence of distinct FHs for these samples, in agreement with the XRPD data discussed above. All samples contain small amounts of Ti_2O_3 (~1 wt%), while the x = 0.2 sample contained 13 wt% of a Fe_2Sn-based phase that is also evident in SEM (below). The Fe_2Sn structure ($P6_3/mmc$; a ~4.23 Å c ~ 5.25 Å) is reported in the ICSD database (entry #103637) but is not identified in the phase diagram [45], suggesting it is metastable, which is consistent with the broad NPD reflections (Fig. 2). This structure has Fe in trigonal bipyramidal (2c-site) and octahedral (2a-site) coordination geometries. Guided by the EDX elemental mapping that indicated the presence of Ti, we allowed for mixed Ti/Fe occupancy and find that the 2c-site has ~50/50 mixed occupancy. Furthermore, the Sn site favours a small deficiency, leading to an overall $Ti_{0.5}Fe_{1.5}Sn_{0.85}$ composition, which is in reasonable agreement with SEM-EDX. The M = Fe composites therefore have a different phase behaviour from the M = Ni samples with no evidence for the presence of a distinct FH phase, even at the relatively high x = 0.2 composition, where a Fe_2Sn-based phase is observed instead. The absence of any obvious Fe containing secondary phases for x = 0.05 and 0.1 initially suggested that most of the Fe had been incorporated in the HH phase. However, Rietveld fits do not show evidence for significant Fe substitution on either the 4c (Co) or 4d (vacant) sites. Our best fits with substitution on the Co site, yielded Fe occupancies of 0.09(1), 0.03(1) and 0.09(1) for x = 0.05, 0.1 and 0.2 (Table 2). These values fall short of the nominal amounts of Fe and it is likely that we do not observe all phases using diffraction.

3.3. Scanning electron microscopy

SEM-EDX data were collected on the M = Ni, x = 0.1 and M = Fe, x = 0.2 samples. Low magnification backscattered electron (BSE) images and EDX elemental maps for the two samples are displayed in Fig. 3. These reveal the presence of significant amounts of secondary phases in these samples, in keeping with the diffraction studies. The elemental maps indicate a strong correlation between Ni-Sn (M = Ni) and Fe-Sn (M = Fe) in the non-HH regions of the sample. Ti, Co and Sb appear homogeneously distributed throughout the HH domains. Oxygen rich-regions are associated with voids observed in both samples and are created during polishing. Small amounts of Ti_2O_3 are evident as small bright spots in the Ti elemental maps, in keeping with the NPD analysis.

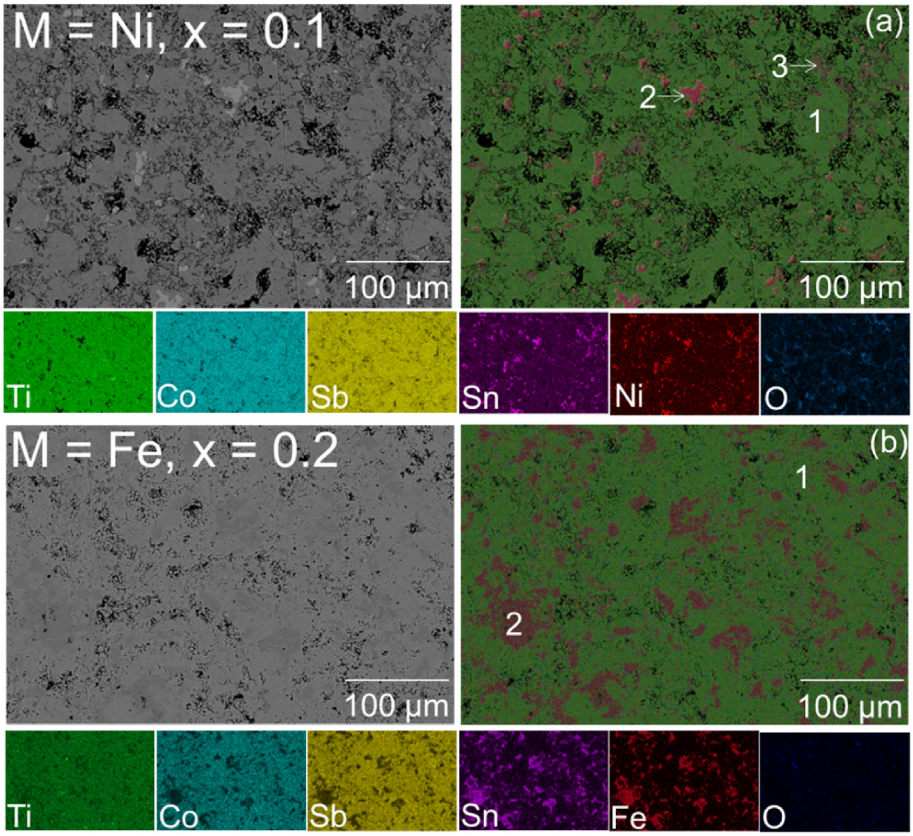

Fig. 3. Backscattered scanning electron microscopy (SEM) images, composite and individual elemental energy dispersive X-ray (EDX) maps for the x = 0.1 M = Ni **(a)** and x = 0.2 M = Fe **(b)** $(TiCoSb)_{1-x}(TiM_2Sn)_x$ Heusler samples. The phases discernible via EDX are as follows: M = Ni sample: 1: the half-Heusler matrix with $TiCo_{0.89(1)}Ni_{0.11(1)}Sb_{0.94(1)}Sn_{0.06(1)}$ composition; 2: Ni_3Sn_2; 3: small amounts of a $Ti_{1.10(5)}(Ni_{0.45(2)}Co_{0.46(2)})_2(Sb_{0.52(2)}Sn_{0.48(2)})_{1.2}$ phase with composition indicative of a full-Heusler phase. For M = Fe: 1: the half-Heusler matrix with $TiCo_{0.91(2)}Fe_{0.09(2)}Sb$ composition and 2: an alloy phase with $Ti_{0.75(2)}Fe_{1.50(6)}Sn_{0.87(4)}$ composition, consistent with the Fe_2Sn-based phase observed in neutron powder diffraction.

The experimental composition of the HH phase in the M = Ni sample is $TiCo_{0.89(1)}Ni_{0.11(1)}Sb_{0.94(1)}Sn_{0.06(1)}$, which is in good agreement with the NPD composition, confirming the substitution of Ni and Sn. Two secondary phases are present: The first is Ni_3Sn_2 (pink regions), which is also evident from diffraction. The second, smaller phase, (purple regions) has a $Ti_{1.10(5)}(Ni_{0.45(2)}Co_{0.46(2)})_2(Sb_{0.52(2)}Sn_{0.48(2)})_{1.2}$ composition, indicative of a FH phase. The HH composition for the M = Fe, x = 0.2 sample is $TiCo_{0.91(2)}Fe_{0.09(2)}Sb$, which agrees well with the NPD composition. A single major secondary phase is evident. This has a $Ti_{0.75(2)}Fe_{1.50(6)}Sn_{0.87(4)}$ composition, which is in reasonable agreement with the fitted composition of the Fe_2Sn phase from NPD. The SEM analysis shows that the bulk of samples consist of a homogenous TiCoSb-based HH, and as discussed below the evolution of the thermoelectric properties can be largely understood by considering the HH phase with a modest influence from the secondary phases.

3.4. Seebeck coefficient, electrical resistivity and power factor

The temperature dependence of ρ, S and S^2/ρ for the M = Ni series are shown in Fig. 4a–c. In all cases, a transition from semiconductor to metal-like conduction occurs. For x = 0.05 and x = 0.1, ρ(T) has a minimum at ~550 K, which reduces to ~510 K for x = 0.15 and ~460 K for x = 0.2. ρ_{313K} systematically decreases from ~12 mΩ cm (x = 0.05) to ~1.8 mΩ cm (x = 0.2). All samples exhibit negative S values, indicating that the conduction is predominantly by electrons. For x = 0.05 and 0.1, S(T) increases with temperature, while it shows a maximum at ~610 K for x = 0.15 and 0.2, indicating the onset of minority charge carrier conduction. The largest $S^2/\rho = 0.8\ mW\ m^{-1}\ K^{-2}$ is observed for x = 0.1 at ~713 K. The onset of minority carrier conduction and downturn in S(T) lead to reduced S^2/ρ values for x = 0.15 and x = 0.2.

The ρ(T), S(T) and S^2/ρ for the M = Fe samples are shown in Fig. 4d–f. Semiconducting ρ(T) are observed for the x = 0.05, 0.1 and 0.2 samples, whilst the most conducting x = 0.15 sample with $\rho_{313K} \sim 4$ mΩ cm shows a transition to metal-like conduction at ~550 K. The S(T) data confirms the n-to p-type transition with $S_{313K} = -100\ \mu V\ K^{-1}$ for x = 0.05 changing to $S_{313K} = +180\ \mu V\ K^{-1}$ for x = 0.1 and decreasing thereafter to $S_{313K} = +60\ \mu V\ K^{-1}$ for x = 0.2, consistent with an increasing p-type carrier concentration. The x = 0.05 sample exhibits a n-to p-type transition upon heating with the crossover at ~540 K, while the other samples are p-type throughout. A maximum $S^2/\rho = 0.8\ mW\ m^{-1}\ K^{-2}$ is obtained for the most highly doped x = 0.2 sample at ~713 K, which is comparable to best performing n-type M = Ni sample (x = 0.1).

3.5. Thermal conductivity and thermoelectric figure of merit

The temperature dependence of κ, κ_{lat} and the figure of merit, ZT for the M = Ni series are shown in Fig. 5a–c. Both κ and κ_{lat} decrease with temperature, as expected for thermal transport limited by point-defect and Umklapp-phonon scattering. $\kappa_{lat,323K} = 7.5\ W\ m^{-1}\ K^{-1}$ for x = 0.1 and decreases to $5.7\ W\ m^{-1}\ K^{-1}$ for the x = 0.15 and 0.2 samples. At 750 K, this decreases to $\kappa_{lat} = 4.2\ W\ m^{-1}\ K^{-1}$ (x = 0.1) and $\kappa_{lat} \sim 3.6\ W\ m^{-1}\ K^{-1}$ for the x = 0.15 and 0.2 samples. Literature data for TiCoSb report $\kappa_{lat,323K} = 18\ W\ m^{-1}\ K^{-1}$ and $\kappa_{lat,750K} = 8\ W\ m^{-1}\ K^{-1}$ [46]. The present samples, therefore have significantly reduced κ_{lat} compared to the TiCoSb parent. The reduced $\kappa_{lat,\ 750K} \sim 4\ W\ m^{-1}\ K^{-1}$ and peak S^2/ρ ~0.8 mW m^{-1} K^{-2} at 713 K for x = 0.1 enable ZT = 0.12 at 713. The x = 0.15 and 0.2 samples with reduced S^2/ρ and larger κ_{el}, due to a reduced ρ, have ZT ~0.09 at 713 K.

The κ(T), κ_{lat}(T) and ZT(T) for the M = Fe series are shown in Fig. 5d–f. Similar trends in κ(T) and κ_{lat}(T) are observed for these samples. $\kappa_{lat,323K} = 10\ W\ m^{-1}\ K^{-1}$ for x = 0.05, decreasing to $8.5\ W\ m^{-1}\ K^{-1}$ (x = 0.1) and $6\ W\ m^{-1}\ K^{-1}$ for x = 0.15 and 0.20. These values are comparable to the M = Ni series ($7.5\ W\ m^{-1}\ K^{-1}$ for x = 0.1 and $5.7\ W\ m^{-1}\ K^{-1}$ for x = 0.1, 0.2), suggesting a similar impact of Fe/Ni substitution and the secondary phases. At 750 K, κ_{lat} tends towards ~6 W m^{-1} K^{-1} for x = 0.05, 0.1 and ~4 W m^{-1} K^{-1} for x = 0.15 and 0.2.

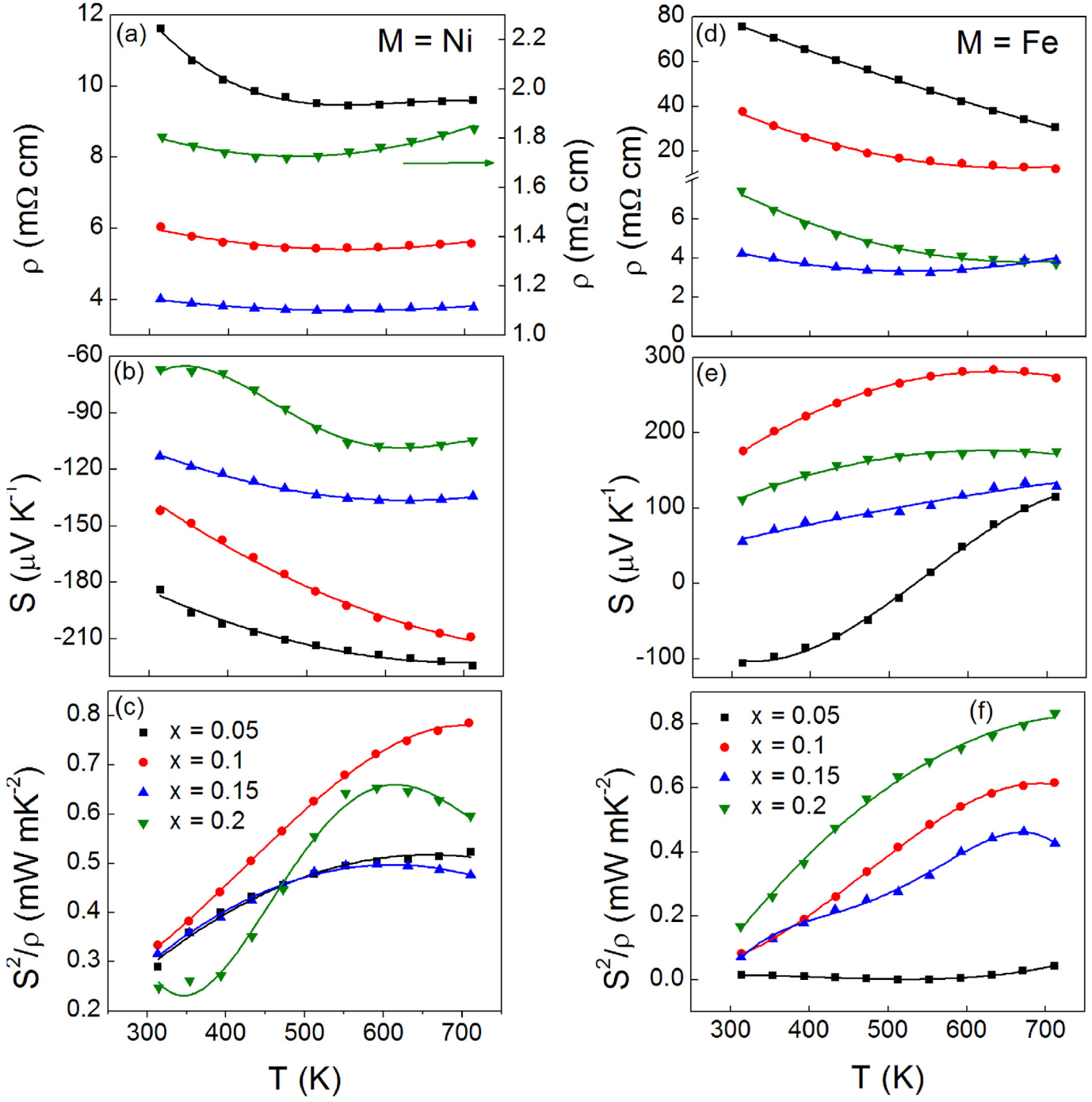

Fig. 4. Temperature dependence of the electrical resistivity (ρ), Seebeck coefficient (S) and power factor (S^2/ρ) for the M = Ni **(a–c)** and M = Fe **(d–f)** $(TiCoSb)_{1-x}(TiM_2Sn)_x$ ($0.05 \leq x \leq 0.2$) Heusler composites. Solid lines are guides to the eye.

For the M = Fe samples, x = 0.2 has the largest S^2/ρ and combined with the low κ_{lat} this results in ZT = 0.12 at 713 K. The peak ZT value for the p-type series is therefore identical to the n-type M = Ni series.

4. Discussion

We have investigated the nominal $(TiCoSb)_{1-x}(TiM_2Sn)_x$ Heusler composites with M = Fe and Ni. Structural analysis reveals direct substitution of Fe and Ni into the HH structure and the formation of a range of FH and non-FH secondary phases. For the M = Ni series, NPD and SEM reveal the presence of Ni_3Sn_2 and an increasing fraction of FH phase. The TiCoSb HH is n-type doped with 13–15% Ni on the Co position for x = 0.1–0.2. In this series, a fraction of the available Ni therefore substitutes in the HH, while the remainder is incorporated in Ni_3Sn_2 and then FH phases. The M = Fe composites show a different behaviour and no FH phase is observed. Instead SEM and NPD point towards the formation of a Fe_2Sn-based structure incorporating some Ti. However, this phase is only clearly observed in the x = 0.2 sample and not for smaller x-values, perhaps due to its metastable nature [45]. NPD affords insight into the composition of the HH phase and indicates Fe/Ni substitution on the Co site. The vacant (4d) site remains unoccupied for both series, and there is therefore no compelling evidence for the presence of interstitials or embedded inclusions.

Despite the deviations from target stoichiometry, the thermoelectric

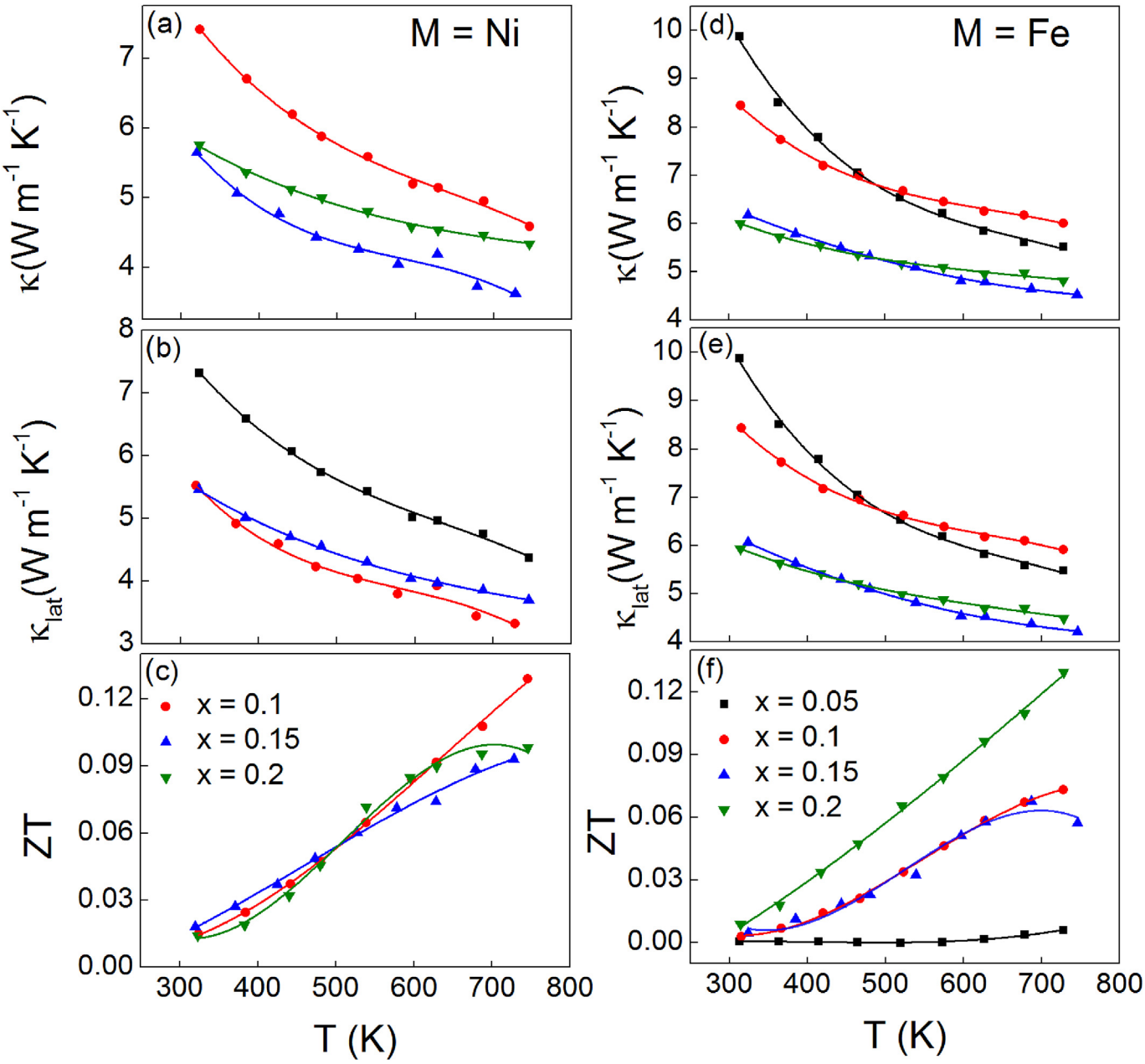

Fig. 5. Temperature dependence of the total thermal conductivity (κ), lattice thermal conductivity (κ_{lat}) and figure of merit (ZT) for the M = Ni **(a–c)** and M = Fe **(d–e)**: $(TiCoSb)_{1-x}(TiM_2Sn)_x$ ($0.05 \leq x \leq 0.2$) Heusler composites. Solid lines are guides to the eye.

properties of the M = Ni and Fe series vary systematically, suggesting they are dominated by the HH phase. An overview of the evolution of S, ρ and κ_{lat} for the M = Ni and Fe series at T ~300 K is given in Fig. 6. For M = Ni (x = 0.1), comparison to literature $TiCo_{1-y}Ni_ySb$ Seebeck coefficient data [47], indicates a Ni content y ~ 0.03, which is smaller than the 13% substitution from NPD, suggesting that the HH phase in our samples also contains Sn, leading to p-type compensation. The EDX composition of the x = 0.1 HH phase ($TiCo_{0.89(1)}Ni_{0.11(1)}Sb_{0.94(1)}Sn_{0.06(1)}$) supports this analysis of compensating n- and p-type doping. The amount of Sn in the HH then decreases as the weight fraction of FH phase increases with our smallest $S = -65\,\mu V\,K^{-1}$ beyond the maximum y = 0.1 with $S = -85\,\mu V\,K^{-1}$ of the literature study [47]. The ρ values are approximately twice those of the literature report, leading to a halving of the maximum power factor, c.f. peak S^2/ρ ~1.5 mW m^{-1} K^{-2} for y = 0.1 [47]. By contrast, κ and κ_{lat} are significantly reduced by ~5 W m^{-1} K^{-1} at 300 K and ~2 W m^{-1} K^{-1} at high-temperature, suggesting increased point defect and boundary phonon scattering, which are more effective at lower temperatures [48]. The reduced κ partially compensates the lower S^2/ρ, leading to a peak ZT = 0.12 at 713 K for our samples, compared to ZT = 0.17 for y = 0.1 [47]. We also considered composite models, but it is difficult to explain the reduction in κ using reasonable estimates for metallic secondary phases. The M = Fe series shows a systematic change from n-to p-type conduction, suggesting that the main change is the doping of the HH phase. The n-to p-type transition occurs near y = 0.02 in $TiCo_{1-y}Fe_ySb$ according to literature data [49] with our $S = -120\,\mu V\,K^{-1}$ for x = 0.05, indicative of <1% Fe substitution. The $S = +180\,\mu V\,K^{-1}$ for x = 0.1 is larger than observed in that study, while the S values for x = 0.15 and 0.2 are consistent with substitution levels 0.05 < y < 0.08 [49]. No Sn substitution was evident from EDX with an approximate composition of $TiCo_{0.91(2)}Fe_{0.09(2)}Sb$ for x = 0.2, where the Fe content is in good agreement with the NPD analysis and the expected value from S. In contrast to the M = Ni series, the ρ values are comparable

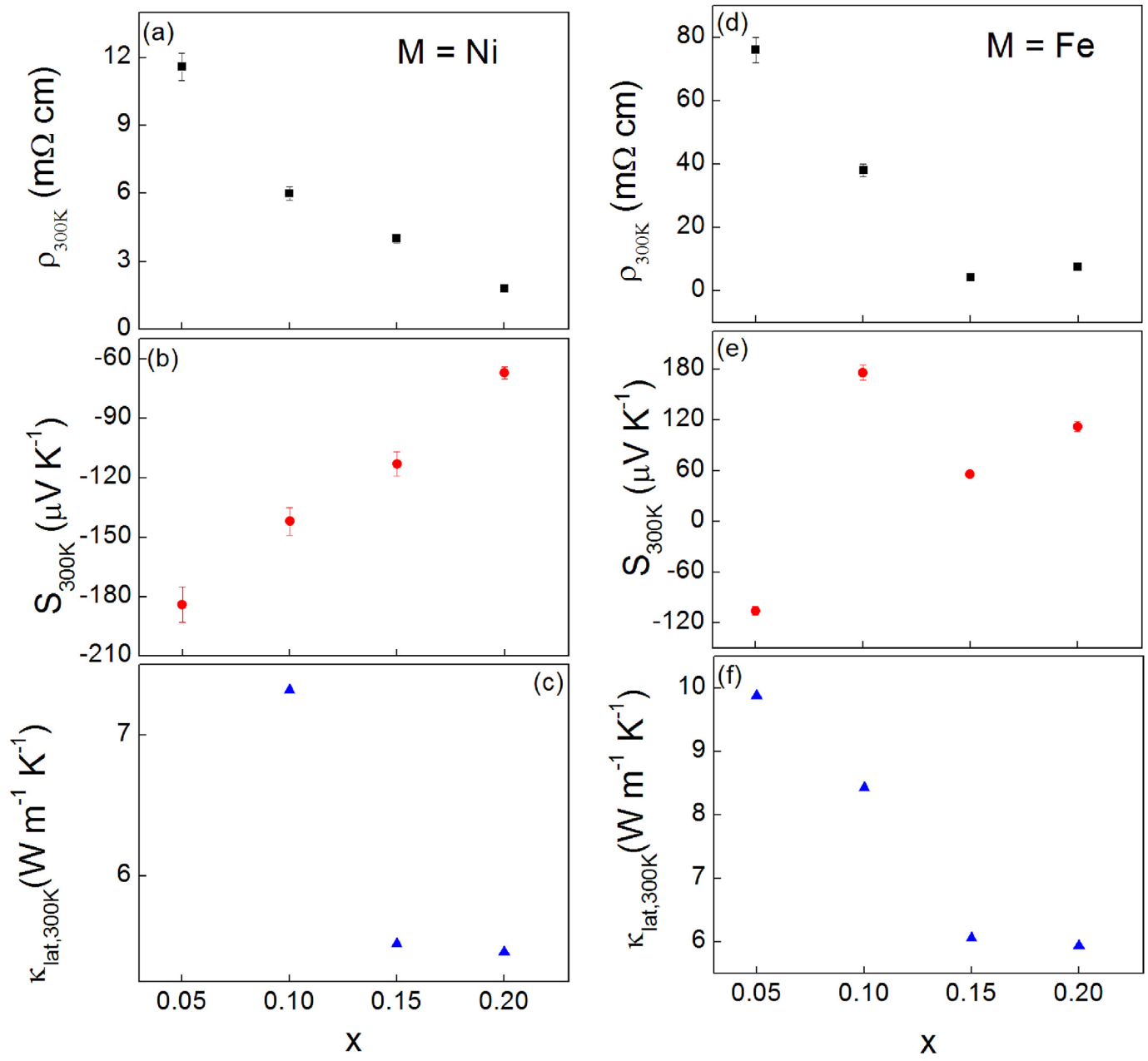

Fig. 6. Composition dependence of the 300 K electrical resistivity (ρ), Seebeck coefficient (S) and lattice thermal conductivity (κ_{lat}) for the M = Ni **(a–c)** and M = Fe **(d–f)** $(TiCoSb)_{1-x}(TiM_2Sn)_x$ ($0.05 \leq x \leq 0.2$) Heusler composites.

to those reported for $TiCo_{1-y}Fe_ySb$, leading to near identical peak $S^2/\rho = 0.9–1$ mW m^{-1} K^{-2} at 713 K for y = 0.08–0.10 [49]. κ and κ_{lat} are suppressed compared to the literature $TiCo_{1-y}Fe_ySb$ samples with ~6 W^{-1} K^{-1} at 300 K for x = 0.15, 0.2, compared to ~10 W m^{-1} K^{-1} for y = 0.1 [49]. As before, the difference at high-temperatures is smaller (~2 W m^{-1} K^{-1}), supporting the notion of increased boundary and point-defect phonon scattering due to the complex microstructure of the samples. Our highest ZT = 0.12 at 713 K is comparable to ZT = 0.13 observed in the literature study for y = 0.1 [49].

This work has explored the $(TiCoSb)_{1-x}(TiM_2Sn)_x$ Heusler composites ($0.05 \leq x \leq 0.2$). Instead of forming two-phase mixtures of HH and FH phases, direct substitution of Ni and Fe into the HH phase occurs, with a variety of secondary FH and non-FH phases observed. The thermoelectric properties are controlled by the HH phase. The samples have moderate power factors and low thermal conductivities, enabling peak ZT ~0.12 in both the p-type (M = Fe) and n-type (M = Ni) series.

Acknowledgements

MA acknowledges the British Council for support. The EPSRC (EP/N01717X/1) is acknowledged for support and the STFC for provision of beam time at ISIS [50]. Raw data underpinning this work is available from the Heriot-Watt data-sharing repository [51].

References

[1] D.M. Rowe, CRC Handbook of Thermoelectrics, CPC Press, Boca Raton, 1995.
[2] D.M. Rowe, Thermoelectrics and its Energy Harvesting, Thermoelectrics and its Energy Harvesting, CRC Press, Boca Raton, 2012.
[3] J.W.G. Bos, R.A. Downie, J. Phys. Condens. Matter 26 (2014) 433201.
[4] S. Chen, Z.F. Ren, Mater. Today 16 (2013) 387–395.
[5] T.J. Zhu, C.G. Fu, H.H. Xie, Y.T. Liu, X.B. Zhao, Adv. Energy Mater. 5 (2015) 1500588.
[6] L. Chen, S. Gao, X. Zeng, A.M. Dehkordi, T.M. Tritt, S.J. Poon, Appl. Phys. Lett. 107 (2015), 041902.

[7] M. Gurth, G. Rogl, V.V. Romaka, A. Grytsiv, E. Bauer, P. Rogl, Acta Mater. 104 (2016) 210–222.
[8] X.A. Yan, G. Joshi, W.S. Liu, Y.C. Lan, H. Wang, S. Lee, J.W. Simonson, S.J. Poon, T.M. Tritt, G. Chen, Z.F. Ren, Nano Lett. 11 (2011) 556–560.
[9] E. Rausch, B. Balke, S. Ouardi, C. Felser, Phys. Chem. Chem. Phys. 16 (2014) 25258–25262.
[10] C.G. Fu, S.Q. Bai, Y.T. Liu, Y.S. Tang, L.D. Chen, X.B. Zhao, T.J. Zhu, Nat. Commun. 6 (2015) 8144.
[11] C.G. Fu, T.J. Zhu, Y.Z. Pei, H.H. Xie, H. Wang, G.J. Snyder, Y. Liu, Y.T. Liu, X.B. Zhao, Adv. Energy Mater. 4 (2014) 1400600.
[12] K. Xia, Y. Liu, S. Anand, G.J. Snyder, J. Xin, J. Yu, X. Zhao, T. Zhu, Adv. Funct. Mater. 28 (2018) 1705845.
[13] D.A. Ferluccio, R.I. Smith, J. Buckman, J.W.G. Bos, Phys. Chem. Chem. Phys. 20 (2018) 3979–3987.
[14] H. Zhu, R. He, J. Mao, Q. Zhu, C. Li, J. Sun, W. Ren, Y. Wang, Z. Liu, Z. Tang, A. Sotnikov, Z. Wang, D. Broido, D.J. Singh, G. Chen, K. Nielsch, Z. Ren, Nat. Commun. 9 (2018) 2497.
[15] S.K. Yee, S. LeBlanc, K.E. Goodson, C. Dames, Energy Environ. Sci. 6 (2013) 2561–2571.
[16] M.W. Gaultois, T.D. Sparks, C.K.H. Borg, R. Seshadri, W.D. Bonificio, D.R. Clarke, Chem. Mater. 25 (2013) 2911–2920.
[17] T. Sekimoto, K. Kurosaki, H. Muta, S. Yamanaka, Mater. Trans. 46 (2005) 1481–1484.
[18] T. Sekimoto, K. Kurosaki, H. Muta, S. Yamanaka, J. Alloys Compd. 394 (2005) 122–125.
[19] T. Sekimoto, K. Kurosaki, H. Muta, S. Yamanaka, J. Alloys Compd. 407 (2006) 326–329.
[20] T. Sekimoto, K. Kurosaki, H. Muta, S. Yamanaka, Mater. Trans. 47 (2006) 1445–1448.
[21] M. Asaad, J. Buckman, R.I. Smith, J.W.G. Bos, RSC Adv. 6 (2016) 56511–56517.
[22] M. Asaad, J. Buckman, J.W.G. Bos, Metals 8 (2018) 935.
[23] S.R. Culp, J.W. Simonson, S.J. Poon, V. Ponnambalam, J. Edwards, T.M. Tritt, Appl. Phys. Lett. 93 (2008), 022105.
[24] V. Ponnambalam, P.N. Alboni, J. Edwards, T.M. Tritt, S.R. Culp, S.J. Poon, J. Appl. Phys. 103 (2008), 063716.
[25] M. Zhou, L.D. Chen, W.Q. Zhang, C.D. Feng, J. Appl. Phys. 98 (2005), 013708.
[26] J.P.A. Makongo, D.K. Misra, X.Y. Zhou, A. Pant, M.R. Shabetai, X.L. Su, C. Uher, K.L. Stokes, P.F.P. Poudeu, J. Am. Chem. Soc. 133 (2011) 18843–18852.
[27] P. Sahoo, Y.F. Liu, J.P.A. Makongo, X.L. Su, S.J. Kim, N. Takas, H. Chi, C. Uher, X.Q. Pan, P.F.P. Poudeu, Nanoscale 5 (2013) 9419–9427.
[28] K. Kirievsky, Y. Gelbstein, D. Fuks, J. Solid State Chem. 203 (2013) 247–254.
[29] Y.W. Chai, Y. Kimura, Appl. Phys. Lett. 100 (2012), 033114.
[30] C.S. Birkel, J.E. Douglas, B.R. Lettiere, G. Seward, N. Verma, Y.C. Zhang, T.M. Pollock, R. Seshadri, G.D. Stucky, Phys. Chem. Chem. Phys. 15 (2013) 6990–6997.
[31] J.E. Douglas, C.S. Birkel, N. Verma, V.M. Miller, M.S. Miao, G.D. Stucky, T.M. Pollock, R. Seshadri, J. Appl. Phys. 115 (2014), 043720.
[32] J.E. Douglas, P.A. Chater, C.M. Brown, T.M. Pollock, R. Seshadri, J. Appl. Phys. 116 (2014) 163514.
[33] Y.W. Chai, Y. Kimura, Acta Mater. 61 (2013) 6684–6697.
[34] R.A. Downie, R.I. Smith, D.A. MacLaren, J.W.G. Bos, Chem. Mater. 27 (2015) 2449–2459.
[35] R.A. Downie, S.A. Barczak, R.I. Smith, J.W.G. Bos, J. Mater. Chem. C 3 (2015) 10534–10542.
[36] R.A. Downie, D.A. MacLaren, R.I. Smith, J.W.G. Bos, Chem. Commun. 49 (2013) 4184–4186.
[37] S.A. Barczak, J.E. Halpin, J. Buckman, R. Decourt, M. Pollet, R.I. Smith, D.A. MacLaren, J.W.G. Bos, ACS Appl. Mater. Interfaces 10 (2018) 4786–4793.
[38] S.A. Barczak, J. Buckman, R.I. Smith, A.R. Baker, E. Don, I. Forbes, J.W.G. Bos, Materials 11 (2018) 536.
[39] W. Jeitschko, Metall. Trans. 1 (1970) 3159.
[40] P.G. Vanengen, K.H.J. Buschow, M. Erman, J. Magn. Magn. Mater. 30 (1983) 374–382.
[41] A.C. Larson, R.B. Von Dreele, Los Alamos National Laboratory Report, LAUR, 2000, 86-748.
[42] B.H. Toby, J. Appl. Crystallogr. (2001) 210–213.
[43] I. Skovsen, L. Bjerg, M. Christensen, E. Nishibori, B. Balke, C. Felser, B.B. Iversen, Dalton Trans. 39 (2010) 10154–10159.
[44] H.-S. Kim, Z.M. Gibbs, Y. Tang, H. Wang, G.J. Snyder, Apl. Mater. 3 (2015), 041506.
[45] Calculated Fe-Sn phase diagram, MTDATA – Phase Diagram Software from the National Physical Laboratory, MTDATA – Phase Diagram Software from the National Physical Laboratory, http://resource.npl.co.uk/mtdata/phdiagrams/fesn.htm.
[46] M. Zhou, L. Chen, W. Zhang, C. Feng, J. Appl. Phys. 98 (2005), 013708.
[47] M. Zhou, C.D. Feng, L.D. Chen, X.Y. Huang, J. Alloys Compd. 391 (2005) 194–197.
[48] E.S. Toberer, A. Zevalkink, G.J. Snyder, J. Mater. Chem. 21 (2011) 15843–15852.
[49] T. Wu, W. Jiang, X. Li, Y. Zhou, L. Chen, J. Appl. Phys. 102 (2007) 103705.
[50] J.W.G. Bos, et al., STFC ISIS Neutron and Muon Source, 2016. https://doi.org/10.5286/ISIS.E.79109693.
[51] M. Asaad, J. Buckman, R.I. Smith, J.-W.G. Bos, Dataset for Phase stability and thermoelectric properties of TiCoSb-TiM2Sn (M = Ni, Fe) Heusler composites, Heriot-Watt University, 2019, https://doi.org/10.17861/0b1f7785-73c6-4d28-9004-90c1ea42a4cf.